Journal of Petroleum Science and Engineering 184 (2020) 106524

Contents lists available at ScienceDirect

Journal of Petroleum Science and Engineering

journal homepage: http://www.elsevier.com/locate/petrol

Impact of shale matrix mechanical interactions on gas transport during production

Guanglei Cui [a], Feng Xia-Ting [a,b,**], Zhejun Pan [c], Tianyu Chen [a,*], Jishan Liu [d], Derek Elsworth [e], Yuling Tan [g], Chunguang Wang [f]

[a] Key Laboratory of Ministry of Education on Safe Mining of Deep Metal Mines, Northeastern University, Shenyang, 110004, China
[b] State Key Laboratory of Geomechanics and Geotechnical Engineering, Institute of Rock and Soil Mechanics, Chinese Academy of Sciences, Wuhan, 430071, China
[c] CSIRO Energy Business Unit, Private Bag 10, Clayton South, VIC, 3169, Australia
[d] School of Mechanical and Chemical Engineering, The University of Western Australia, 35 Stirling Highway, Perth, WA, 6009, Australia
[e] Department of Energy and Mineral Engineering, G3 Center and Energy Institute, The Pennsylvania State University, University Park, PA16802, USA
[f] Key Laboratory of Tectonics and Petroleum Resources, China University of Geosciences, Wuhan, 430074, China
[g] State Key Laboratory of Mining Disaster Prevention and Control Co-founded by Shandong Province and the Ministry of Science and Technology, Shandong University of Science and Technology, China

ARTICLE INFO

Keywords:
Effective diffusion
Surface diffusion
Organic matter
Inorganic minerals
Effective stress

ABSTRACT

Shale gas has played an increasingly important role in world energy supply in recent years. The gas transport process in the shale matrix is particularly important as it affects the long-term production behavior of shale gas. The shale matrix consists of inorganic minerals and embedded organic matter with mass transfer influenced by mechanical interactions. We develop a micro-scale discrete coupled model to explicitly account for mass transfer and mechanical interactions, and how these interactions affect the gas transport characteristics of both components. Specifically, the model comprises organic matter embedded within inorganic minerals. The proposed model is implemented and solved within the framework of COMSOL Multiphysics (Version 5.4). The model is first verified against the results of a desorption-diffusion-seepage coupled experiment and then extended to field scale. It is found that the impacts of gas pressure and effective strain are different for the gas seepage in inorganic minerals and gas diffusion in organic matter. Gas pressure may enhance the permeability of the inorganic phase due to the gas slippage effect while compactive effective strain decreases permeability during the gas depletion process. For gas diffusion in the organic matter, surface diffusion decreases and effective diffusion coefficient increases with declining gas pressure. While the impacts of effective strain on the effective diffusion are dependent on the external boundary conditions, the effective diffusion coefficient is lower than the initial value under constant stress conditions and larger than the initial value under constant volume conditions. The proposed model provides a complementary method to conventional continuum dual-media approaches and provides a clear understanding of the interactions between the two components. Field-observed oscillatory gas production data is readily history-matched and key mechanisms explained with the proposed approach presented in this work.

1. Introduction

Unconventional resources, especially shale gas, play an increasingly indispensable role in current energy supply due to its huge reserves and increasing production (EIA, 2016). Contrary to conventional reservoirs, the shale matrix exhibits a highly heterogeneous pore structure ranging from nanoscale (intragranular pore in kerogen) to micrometer scale (natural fracture) and is composed of inorganic minerals encasing embedded organic matter. The contrasting flow characteristics and mechanical properties between these two components are huge, resulting in coupled controls in mass transfer and mechanical interactions between them. Most previous studies (Zhao et al., 2014; Peng et al., 2015; Cui et al., 2018a) simplified the two interaction terms as solely a function of the gas pressure difference and ignored the impact of

* Corresponding author.
** Corresponding author. Key Laboratory of Ministry of Education on Safe Mining of Deep Metal Mines, Northeastern University, Shenyang, 110004, China.
E-mail addresses: fengxiating@mail.neu.edu.cn, xia.ting.feng@gmail.com (F. Xia-Ting), chentianyu@mail.neu.edu.cn (T. Chen).

https://doi.org/10.1016/j.petrol.2019.106524
Received 23 February 2019; Received in revised form 14 August 2019; Accepted 23 September 2019
Available online 25 September 2019
0920-4105/

pressure and strain transfer within the inner structure of the two components. However, this knowledge is important in the understanding of shale gas production behavior.

Scanning electron microscopy (SEM) (Loucks et al., 2009), and transmission electron microscopy (TEM) (Javadpour, 2009) are typically applied to study the pore structure of the shale matrix (Chen et al., 2013; Mehmani et al., 2013). Shale structure may be defined through 2-D and 3-D submicron-scale images of shales using Focused Ion Beam (FIB)/SEM imaging (Ambrose et al., 2010). In these images, finely-dispersed porous organic matter (kerogen inclusions) is observed to be embedded within the inorganic matrix. The inorganic matrix may contain larger-size pores of varying geometries. The nano-scale intragranular pore, intergranular pore in organic matter and micro-scale fracture in inorganic minerals are also all observed in the literature (Loucks et al., 2012; Tian et al., 2013; Yang et al., 2014; Chen et al., 2015b; Song et al., 2015). These observations indicate that the shale reservoir is characterized by complex and multi-scale pore geometry and that the gas transport characteristics in the two components exhibit significant structural differences controlling mass transfer term between them.

Besides the heterogeneity of the gas flow behavior, the heterogeneous distribution of mechanical properties in the shale matrix is also important. Atomic force microscopy (AFM) and its PeakForce Quantitative Nano-mechanical Mapping (Peak-Force QNM™) mode provide a convenient way to calculate Young's modulus of different components in the shale matrix at nano-scale. AFM was used to map the mechanical properties of organic and inorganic components (Eliyahu et al., 2015) defining Young's modulus of the organic matter ranging from 0 to 25 GPa while that of inorganic minerals ranging up to 60 GPa. Similar methods (Emmanuel et al., 2016) were applied to investigate the impact of thermal maturation on nano-scale elastic properties of organic matter. When vitrinite reflectance increases from 0.40 to 0.82, the average Young's modulus of organic inclusions increases from 6.1 GPa to 16.0 GPa (Emmanuel et al., 2016). The above studies indicate that the mechanical behavior of the inorganic minerals and the organic matter during the gas flow process are different due to the heterogeneity of the mechanical properties.

Multi-porosity models are widely applied for the gas flow simulation, including the original dual-porosity/dual-permeability (DP/DK) model (Warren and Root, 1963). In the DP/DK model, the gas reservoir is conceptually separated into the fracture system and matrix system, with the two systems interacting via a mass transfer term. However, the DP/DK model cannot accurately describe gas flow in the multi-scale pore geometry of real shale gas reservoirs (Castillo et al., 2011; Pan and Connell, 2015). Furthermore, hydraulic fracturing may activate some previously non-connected and thus non-effective porosities, and the dual-porosity reservoir may be transformed into a triple-porosity or multi-porosity system (Gale et al., 2007; Rogers et al., 2010). In these models, a more complex geometry structure and mass transfer term are assumed (Abdassah and Ershaghi, 1986; Haghshenas et al., 2013). As an important supplement, the impacts of gas-solid coupling processes on the gas flow are considered. Sequential gas flow models considering different flow regimes in different pores are a viable characterization (Peng et al., 2015) where the concept of effective strain is modified to permeability change resulting from both flow regimes and stress variation. Conversely, a triple-permeability model in which the shale matrix is composed of the inorganic system and an embedded organic system is considered in Cui's work (2018a). The model can accommodate the impacts of the mass transfer and effective stress transfer between different components. It should be noted that most coupled models follow continuum approaches in which each node represents several nested systems and the sub-systems in the shale matrix are assumed homogeneous. In this approach, the interactions between the sub-systems are simplified as the average gas pressure difference between them and the impact of the pressure gradient and stress gradient in the interior of the two components are not fully considered.

Previous studies have shown that the shale matrix contains inorganic minerals and embedded organic matter (Ambrose et al., 2010a; Akkutlu and Fathi, 2012; Wasaki and Akkutlu, 2014; Chen et al., 2015b) and that properties of both mechanical and gas transport characteristics exhibit strong heterogeneity (Loucks et al., 2012; Tian et al., 2013; Eliyahu et al., 2015). While in traditional continuum methods (multi-porosity models) the interactions between inorganic minerals and organic matter are simply treated as a function of the average gas pressure difference. In this work, based on the geometric structure and associated mechanical and transport properties, a discrete micro-scale coupled model is proposed to investigate the impact of shale matrix heterogeneity on gas flow characteristics. In this model, the inorganic minerals and organic matter interact with both mass transfer and strain transfer. The model is solved numerically through COMSOL Multiphysics (Version 5.4). The numerical modeling results are validated against experimental data and parameter sensitivity studies are performed. Then the evolution of gas flow characteristics of both organic matter and inorganic minerals are evaluated accommodating the impacts of both gas pressure and mechanical deformation.

2. Mathematical model

The development of horizontal drilling and multi-stage hydraulic fracturing technologies have first enabled and then enhanced gas production from shale reservoirs. During the fracturing process, hydraulic fluid, proppants, and activators are injected into the shale reservoir. The proppants maintain the fracture open to enhance gas production during the gas depletion process (Tan et al., 2017, 2018). As mentioned above the shale matrix contains inorganic minerals and organic matter with Fig. 1 presenting a typical high-resolution SEM image of shale matrix (Ambrose et al., 2010a; Akkutlu and Fathi, 2012; Wasaki and Akkutlu, 2014). As shown in the figure, organic inclusions are distributed in the shale matrix as complex and inter-connected nanopores (Ambrose et al., 2010; Curtis et al., 2012; Yang et al., 2016). Gas is stored within the organic inclusions as both free gas and adsorbed gas. After hydraulic fracturing, a sequence of gas flow occurs (Peng et al., 2015); first, the gas in the inorganic mineral pores flows to the fracture which is usually described by modified Darcy flow, then the gas in the organic matter begins to diffuse as the main contributor to the long-term production.

2.1. The concepts of heterogeneous deformation in shale matrix

As shown in Fig. 1, the shale matrix consists of two major constituents: inorganic minerals and organic matter. In this section, a small representative unit sufficiently large to represent the essential feature of the shale matrix is selected to investigate the interaction between two sub-systems during the gas production process (Fig. 2). In this work, constant stress and constant volume conditions are selected as representative boundary conditions for the system. The constant volume condition means the whole volume of the representative unit is kept invariant. In such condition, the whole representative unit cannot deform in both horizontal and vertical planes while the relative deformation of the organic matter and inorganic mineral inside the representative unit can occur. For the constant stress condition, the confining stress applied on the outer boundary is kept invariant during the gas depletion/injection process. In such condition, the representative unit can swell or deform freely. These two representative boundary conditions are selected for three reasons: (1) The gas reservoir is assumed horizontal and is acted on by an invariant overburden stress. Therefore, two assumptions are commonly made for the gas reservoir simulation: uniaxial strain and constant overburden stress (Pan and Connell, 2012). The former one defines that the strain within the horizontal plane is zero but vertical strain could change (Shi and Durucan, 2004). Constant overburden stress means that the invariant stress overlies a reservoir and is calculated on the weight of the overburden geology (Shi and Durucan, 2004). In such assumptions, the mechanical condition in the horizontal

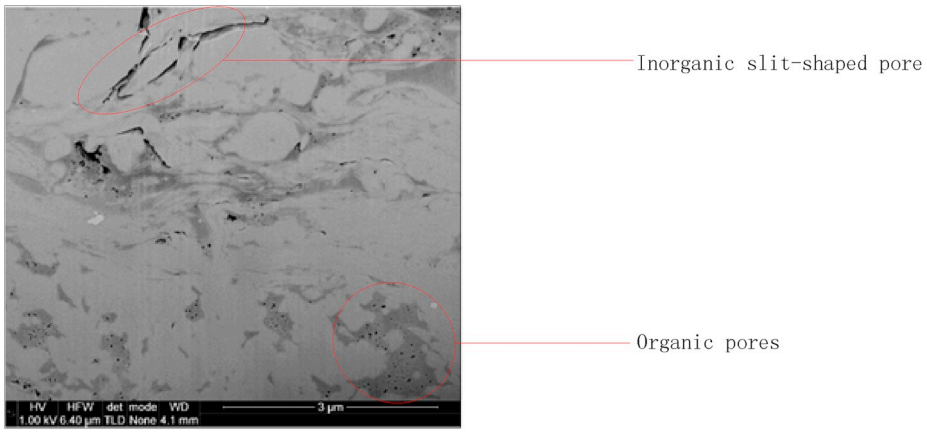

Fig. 1. SEM image of shale matrix (Ambrose et al., 2010a; Akkutlu and Fathi, 2012; Wasaki and Akkutlu, 2014).

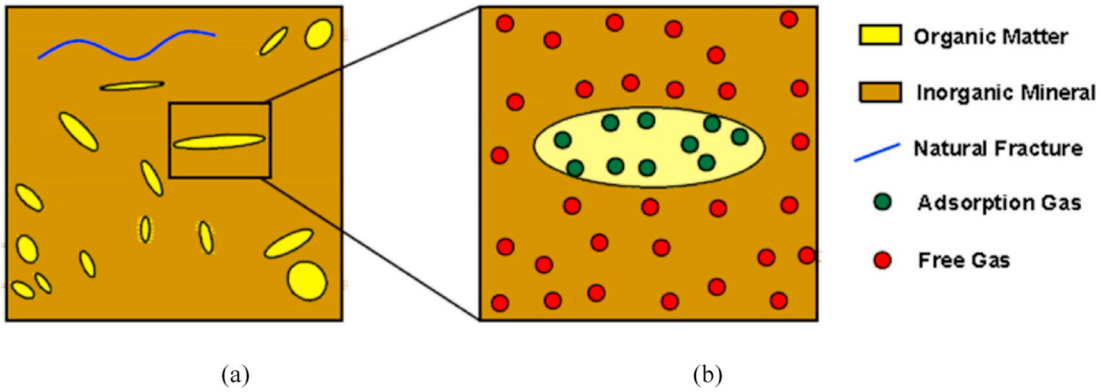

Fig. 2. The image of a representative elemental volume (REV). (a) distribution of inorganic minerals and organic matter; (b) gas storage state.

direction can be assumed as the constant volume condition with a constant stress condition in the vertical direction (Liu et al., 2011b); (2) Also these two boundary conditions are easily obtained and usually applied in the lab (Li et al., 2009; Ma et al., 2011; Chen et al., 2015a, b; Kumar et al., 2016; Wang et al., 2017a; Wang et al., 2019; Cui et al., 2018b); (3) Furthermore, as demonstrated and discussed in our previous work, these two boundary conditions correspond to the extreme limits of permeability evolution (Liu et al., 2011a; Cui et al., 2018b; Shi et al., 2018) – prescribed stress or prescribed deformation. Taking the gas injection process as an example, the constant volume condition represents the lower limit (maximum permeability reduction with swelling and converse with shrinkage) while the constant stress condition represents its upper limit. Permeability evolution under intermediate boundary conditions are located between these two extremes (Peng et al., 2017). These two boundary conditions are also widely adopted in our previous work (Liu et al., 2011a, 2011b; Cui et al., 2018b).

2.1.1. The deformation of representative elemental volume (REV) under the constant stress condition

The gas depletion process of adsorbed gas (CH_4) is illustrated as an example to investigate the deformation of the representative unit under the constant stress condition. Before depletion, the shale matrix is at equilibrium state and no interaction between organic matter and inorganic minerals exists as shown in Fig. 3(a). The gas depletion process can be summarized as three stages: (1) In the initial gas production stage, the gas pressure in the inorganic matrix reduces rapidly. Based on the effective stress principle, the inorganic minerals are compressed together with the organic matter as a result of strain transfer. Therefore, both inorganic minerals and organic matter are compressed in this stage as illustrated in Fig. 3(b); (2) In the second stage, free gas in the inorganic minerals are further depleted. Due to the extremely low transportability of the organic matter, a large gas pressure difference forms at the boundary between the two sub-systems. Due to the large gradient, the boundary extends and the organic matter may swell as illustrated in Fig. 3(c); (3) In the final stage, both the adsorbed gas and free gas in the organic matter are fully depleted, as illustrated in Fig. 3 (d). During this stage, the pore volume of the organic matter is determined by the competing mechanisms between the declining gas pressure and gas desorption. The former term would decrease the pore volume according to the effective stress principle while the latter term enlarges the pore volume.

2.1.2. Deformation of REV under the constant volume condition

Similarly, the gas depletion process of adsorbed gas (CH_4) is used to demonstrate the deformation of the REV under the constant volume condition. Before depletion, the shale matrix is at equilibrium state, as shown in Fig. 4(a). Again, three stages can be observed: (1) In the initial stage, the gas pressure in the inorganic matrix rapidly declines. The relative volumes of the organic matter and inorganic minerals change as the stress equilibrium state between the two components is disturbed as shown in Fig. 4 (b). The volume of inorganic mineral decreases because of the declined gas pressure in itself while the organic matter swells due to its relative larger gas pressure and invariant volume of the whole REV; (2) Also in the second stage, a large pressure gradient develops on the boundary between the two components. Under this condition, the organic matter swells while the inorganic mineral fraction is further compressed, as illustrated in Fig. 4(c); (3) In the final stage, the pore volume of the organic matter is mainly determined by internal processes: the decreased gas pressure and gas desorption. As discussed above, organic matter has different responses to different outer

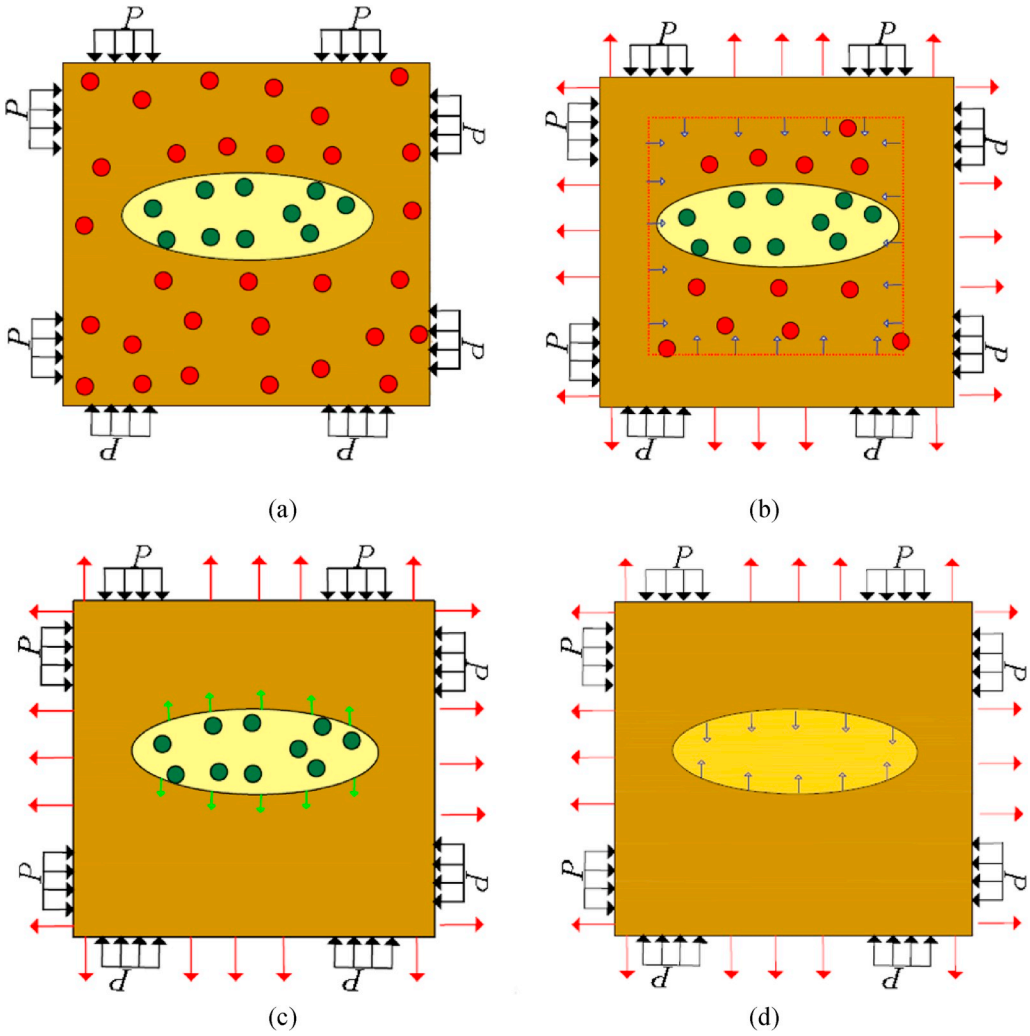

Fig. 3. Deformation of the representative elemental volume (REV) during gas depletion under the constant stress condition. The red arrow shows the gas flow direction, the blue and green arrows represent the deformation of inorganic mineral and organic matter, respectively. (a) initial state: equilibrium state; (b) first stage: a portion of the gas in the inorganic minerals flows out; (c) second stage: gas in the inorganic minerals fully depletes; (d) final state: gas in organic matter flows out. (For interpretation of the references to colour in this figure legend, the reader is referred to the Web version of this article.)

boundary conditions in the first gas depletion stage. The volume of organic matter decreases under the constant stress condition and increases under constant volume condition.

2.2. Governing equation for the mechanical process in shale matrix

Based on thermodynamics and poroelasticity theory, the governing equation of the mechanical deformation is obtained as (Heidug and Wong, 1996; Coussy, 2004):

$$\dot{\sigma}_{ij} = (K - \frac{2G}{3})\dot{\varepsilon}_{kk}\delta_{ij} + 2G\dot{\varepsilon}_{ij} - \xi\dot{p}\delta_{ij} + \sum_k \omega^k \dot{\mu^k}\ \delta_{ij} \tag{1}$$

in which ε_{ij} represents infinitesimal strain, σ_{ij} represents the Cauchy stress, G represents the shear modular, K represents the bulk modulus, δ_{ij} is the Kronecker delta, p is the fluid pressure, μ^k is the chemical potential of the fluid phase, ω^k is a coefficient relating to the dual derivative of potential to the chemical potential and strain, superscript k is the index of the fluid type, the superscript dot represents the increment with time and the quantity ξ is the Biot coefficient.

The adsorption stress σ_a acting on the pore walls should be accommodated if the porous medium is saturated with an adsorptive fluid. The integral form of Eq. (1) can be written as:

$$\sigma_{ij} = (K - \frac{2G}{3})\varepsilon_{kk}\delta_{ij} + 2G\varepsilon_{ij} - \xi p\delta_{ij} + \sigma_a \tag{2}$$

in which

$$\sigma_a = \int_{t_0}^{t} \sum_k \omega^k \mu^k \delta_{ij} dt \tag{3}$$

If the chemical potential at time t_0 and time t are known, Eq. (3) can be transformed into:

$$\sigma_a = \int_{\mu_0}^{\mu} \sum_k \omega^k \mu^k \delta_{ij} d\mu = \int_{\mu_0}^{\mu} \sum_k \Gamma(\mu) du_k \tag{4}$$

under the assumption that the gas potential density Γ(μ) does not depend on the deformation of the surface. Usually, the Langmuir adsorption isotherm is widely used and written as $n^a = \frac{LBP}{1+BP}$ in which B is the Langmuir pressure constant and L is the Langmuir mass constant. Therefore:

$$\Delta\sigma_s = \int_{p_0}^{p} \chi' \frac{LBP}{1+BP} d(RT \ln p) = RTL\chi' (\ln(1+Bp) - \ln(1+Bp_0)) \tag{5}$$

in which χ' is a constant parameter depending on the topological structure and can be obtained from experimental observations (Chen et al., 2018). We can obtain the equation as follows (Pan and Connell, 2007; Vandamme et al., 2010):

$$\sigma_{ij} = (K - \frac{2G}{3})\varepsilon_{kk}\delta_{ij} + 2G\varepsilon_{ij} - \xi p\delta_{ij} - RTL\chi' \ln(1+Bp) \tag{6}$$

From the preceding, the mechanical equations for the inorganic minerals and organic matter can be obtained as (Zhang et al., 2018):

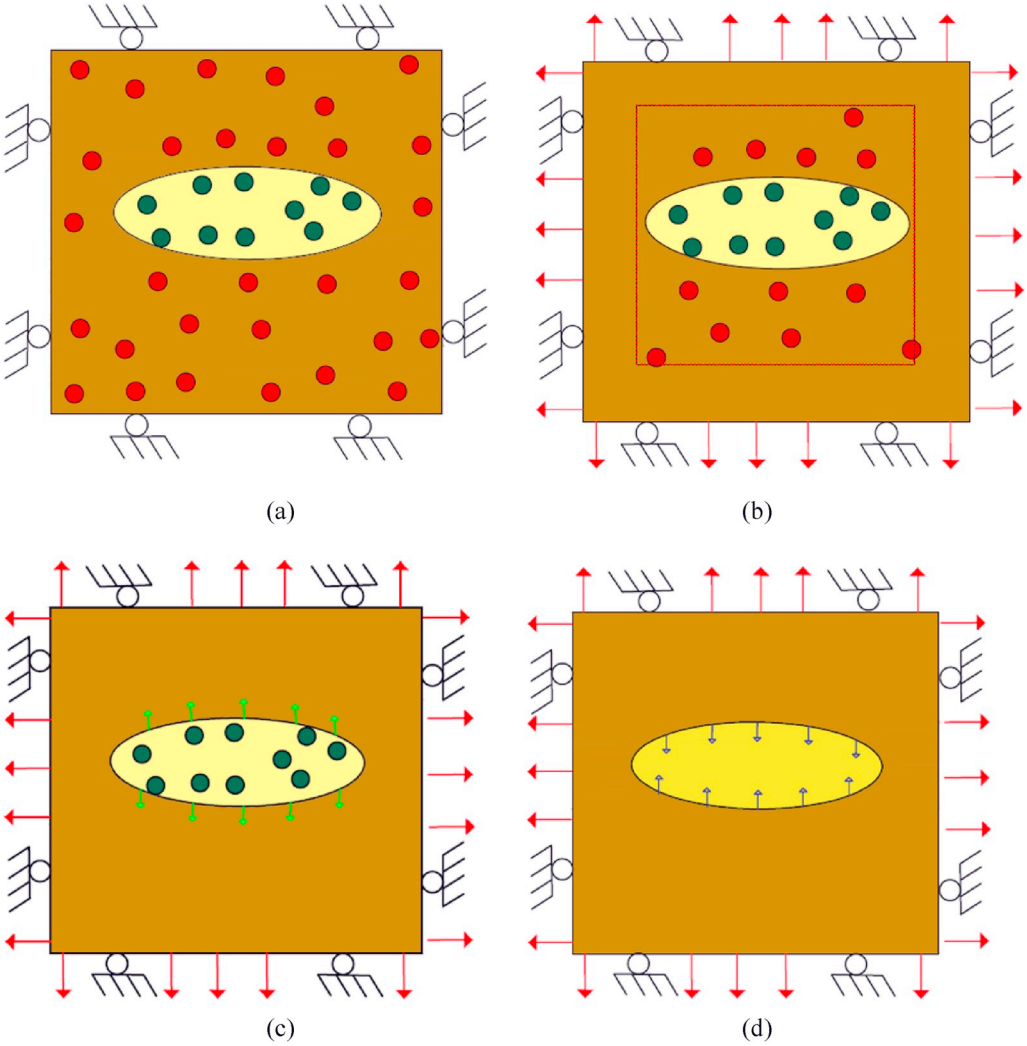

Fig. 4. Deformation of the representative elemental volume (REV) under the constant volume condition. The red arrow represents the gas flow direction, the blue and green arrows represent the deformation of the inorganic mineral and organic matter, respectively. (a) initial state: equilibrium state; (b) first stage: a portion of the gas in the inorganic mineral flows out; (c) second stage: the gas in the inorganic mineral depletes fully; (d) final state: the gas in the kerogen inclusions is fully depleted. (For interpretation of the references to colour in this figure legend, the reader is referred to the Web version of this article.)

$$Gu_{i,kk} + \frac{G}{1-2v}u_{k,ki} = \alpha_{in}p_{in,i} + f_{or2in} \tag{7.a}$$

$$Gu_{i,kk} + \frac{G}{1-2v}u_{k,ki} = \alpha_{or}p_{or,i} + RTL\chi^{'}\ \ln(1+Bp_{or}) + f_{in2or} \tag{7.b}$$

in which subscripts *or* and *in* represent organic matter and inorganic mineral, and f_{in2or} and f_{or2in} represent the interaction force between the two components with $f_{in2or} + f_{or2in} = 0$.

2.3. Gas flow in shale matrix

2.3.1. Modified Darcy flow in inorganic minerals

The gas flow regime in the inorganic minerals is significantly different from that in conventional reservoirs because of the smaller pore diameter and the invalidity of the continuity assumption (Tan et al., 2019). The apparent permeability approach utilizing a modified Darcy equation is proposed to account for this inconsistency (Javadpour, 2009; Azom and Javadpour, 2012; Darabi et al., 2012). In the apparent permeability model (APM), the permeability is written as $k_{in} = f(Kn)\ k_{in\infty}$. The first term $f(Kn)$ represents the correction factor for gas slippage which is usually a function of the Knudsen number (Kn) and $k_{in\infty}$ represents the intrinsic permeability of the inorganic system. The governing equations of the modified Darcy flow in inorganic minerals is included in Appendix A.

2.3.2. Gas diffusion in organic matter

Following gas depletion, the gas contained in the organic matter diffuses into the inorganic pores driven by the concentration difference, although which diffusion term as the dominant mechanism remains debatable (Azom and Javadpour, 2012; Darabi et al., 2012).

Diffusion in porous media can be categorized as bulk flow, Knudsen flow, and transition flow (Roy et al., 2003) based on the Knudsen number (Kn) although these distinctions exclude the occurrence of transition zones. To overcome the limitation of flow regime classification, the unified effective diffusion model uses weighting and probability function methods to represent behavior. In the first approach, the diffusion mass transport term is written as a weight of the bulk diffusion and Knudsen diffusion (Dongari et al., 2009; Geng et al., 2016). In the second approach, the probability function is proposed to account for the different contributions of diffusion regime (Scott and Dullien, 1962; Wakao et al., 1965; Hashemifard et al., 2013a).

For adsorbed gas, the gas molecules are driven by the chemical gradient of the adsorbed phase and flow along the wall surface. This flow regime represents one of surface diffusion (Fathi and Akkutlu, 2009) which is an activated process changing with gas pressure. The governing equations for gas diffusion in the organic matter are as noted in Appendix B.

2.4. Solid-gas coupled model

2.4.1. Porosity and permeability model of inorganic minerals

The porosity of the inorganic mineral is related to the effective strain (Peng et al., 2014):

$$\frac{\phi_{in}}{\phi_{in0}} = 1 + \frac{\alpha_{in}}{\phi_{in0}} \Delta\varepsilon_{ine} \tag{8}$$

whereϕ_{in0} is the initial porosity and α_{in} is the Biot coefficient of the mineral matrix. The effective strain (ε_{ine}) is the sum of global strain (ε_{ing}) and local strain (ε_{inl}) of the inorganic system:

$$\Delta\varepsilon_{ine} = \Delta\varepsilon_{ing} + \Delta\varepsilon_{inl} \tag{9}$$

The global strain of the mineral matrix is the resultant of the volumetric strain (ε_{inv}) of inorganic minerals and the internal strain (ε_{or2in}) induced by the interaction between inorganic mineral and organic matter:

$$\Delta\varepsilon_{ing} = \Delta\varepsilon_{inv} + \Delta\varepsilon_{or2in} \tag{10}$$

The local strain of the inorganic mineral is applied as the compressive strain of the gas pressure itself (also called pressure strain in this work):

$$\Delta\varepsilon_{inl} = \frac{\Delta p_{in}}{K_{ins}} \tag{11}$$

where K_{ins} is the bulk modulus of the inorganic mineral skeleton.

A typical relationship between porosity and permeability is the cubic law (Zhang et al., 2008):

$$\frac{k_{in}}{k_{in0}} = \left(\frac{\phi_{in}}{\phi_{in0}}\right)^3 = \left(1 + \frac{\alpha_{in}}{\phi_{in0}} \Delta\varepsilon_{ine}\right)^3 \tag{12}$$

and may be used to represent the evolution of the flow characteristics of the system.

2.4.2. Porosity and permeability model of organic matter

Similarly, the porosity of the organic matter is related to the effective strain:

$$\frac{\phi_{or}}{\phi_{or0}} = 1 + \frac{\alpha_{or}}{\phi_{or0}} \Delta\varepsilon_{ore} \tag{13}$$

where ϕ_{or0} is the initial porosity and α_{or} is the Biot coefficient of the organic matter. The effective strain $\triangle\varepsilon_{ore}$ also includes the global strain (ε_{org}) and local strain (ε_{orl}) of organic matter:

$$\Delta\varepsilon_{ore} = \Delta\varepsilon_{org} + \Delta\varepsilon_{orl} \tag{14}$$

The global strain of the organic matter is the combination of the volume strain of the organic matter (ε_{orv}) and the internal strain induced by the interaction between the two components (ε_{or2in}):

$$\Delta\varepsilon_{org} = \Delta\varepsilon_{orv} - \Delta\varepsilon_{or2ke} \tag{15}$$

The local strain of the organic matter contains the adsorptive strain (Chen et al., 2015b; 2018) and the compressive strain due to gas pressure (also called pressure strain):

$$\Delta\varepsilon_{orl} = \frac{\Delta p_{or}}{K_{ors}} + RTL\chi'\left(\ln(1 + Bp_{or}) - \ln(1 + Bp_{or0})\right) \tag{16}$$

where K_{ors} is the bulk modulus of the organic matter.

3. Model validation

In this section, the fully coupled model described above is applied to history match experimental data (Guo et al., 2015). The procedure and results of the model validation are reported in this section.

3.1. Numerical model

For the geometry of the simulation model, we assume that the natural fractures are located at the infinity and surround the representative unit. In such condition, the influences of the outer mechanical boundary and gas flow boundary are uniform equidistant to the points with the same distance to the center of the representative unit (REV). Based on that assumption, a spherical geometry is selected for both components as shown in Fig. 5 (a). Due to symmetry, only 1/8 of the sphere is modeled as shown in Fig. 5 (b), and both the gas flow and mechanical symmetric boundary conditions are applied on the inner boundary. The *x-y* plane projection is used to illustrate the gas flow and mechanical boundary conditions as shown in Fig. 5 (c) and Fig. 5 (d), respectively. For the gas flow models, the flow boundary conditions are given as:

$$p_{or} = p_{in} \text{ on } \partial\Omega \tag{17}$$

for the interface between the organic matter and inorganic minerals, and

$$p_{in} = p_{out} \text{ on } \partial\Omega \tag{18}$$

for the outer edge acting as the extraction pressure.

To represent the constant stress condition, the outer boundaries are free to deform under invariant confining stress as shown in Fig. 5 (c). To represent the constant volume condition, displacement on outer boundaries is fixed as shown in Fig. 5 (d). For the interface between the organic matter and inorganic minerals, it should satisfy the equation of strain compatibility and the applied stress is continuous.

3.2. Desorption-diffusion-seepage coupled experiment

Guo et al. (2015) conducted a gas desorption-diffusion-seepage coupled experiment to measure the Technically Recoverable Resources (TRR). The core sample was collected from the lower Silurian Longmaxi Formation of the Sichuan basin, south China, from a depth of 1048 m. The porosity is 0.4% and the permeability $\sim 2 \times 10^{-20} m^2$. No visible fracture was observed in the sample. Gas desorption was conducted in the experiment with a saturated gas pressure of 29 MPa and a confining pressure of 40 MPa. Initial methane saturation lasted 240 days to ensure a state of full saturation. Then an extraction pressure of 2 MPa was applied to the core holder to simulate the gas situation. The gas rates were recorded and are displayed in Fig. 6.

3.3. Model validation process

As observed in Fig. 6, the flow rates measured in the experiment are not zero at the conclusion of the experiment. In this work, the Gaussian Decomposition Method (Cui et al., 2018c) is used to fit the experimental data where goodness of fit is up to 99.21% as shown in Fig. 6. From this approach, the end time (t_{end}) of gas depletion can be obtained, and the total gas amount (Q_{total}) recovered can also be determined from the integral form of the Gaussian function. In a further step, the dimensionless time and dimensionless gas flow rate are used for model validation. The dimensionless time is defined as $t_\tau = t/t_{end}$ and the dimensionless gas flow rate is defined as $q_\tau = Q_t/Q_{total}$ in which Q_t is gas production amount between the time interval $2\triangle t$ and defined as $Q_t = \int_{t-\Delta t}^{t+\Delta t} q_t dt$. For better verification, three major assumptions are made in this work: (1) the shale sample is assumed to comprise inorganic minerals and organic matter as no visible fractures are observed in the sample; (2) an REV can always be found representing the permeability variation and gas depletion behavior of the entire sample; and (3) the impact of the boundary conditions on the sample has the same impact on the REV. These three assumptions are also adopted in our previous work (Cui et al., 2018b). Then the fully coupled model mentioned above is applied to history match the experimental results. The Wakao method is used to calculate the effective diffusion coefficient in the organic matter. The parameters are listed in Table 1 and the fitting results are shown in

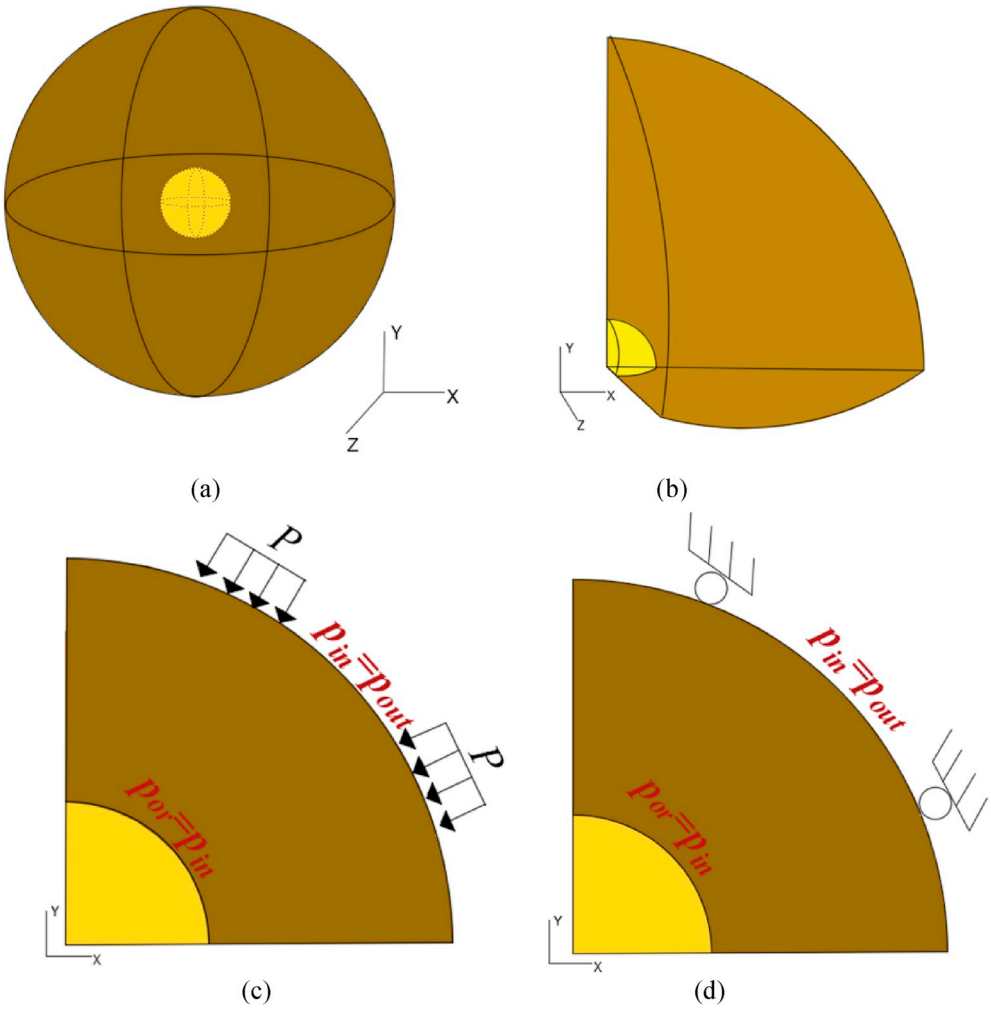

Fig. 5. Numerical model for the REV. (a) distribution of organic matter and inorganic minerals; (b) 1/8 section of the sphere; (c) boundary conditions under constant stress; (d) boundary conditions under the constant volume condition.

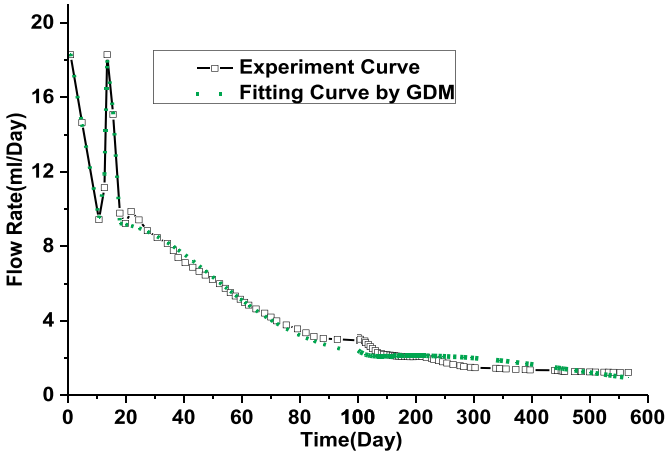

Fig. 6. Experimentally-measured flow rate.

Fig. 7. Generally, a satisfactory result is obtained.

The contributions of different components to the gas flow rate are also illustrated in Fig. 7. As shown in the image, the gas in the inorganic minerals first exits and is characterized by a high flow rate then declines rapidly. When extraction pressure front reaches the organic matter, the organically-stored gas begins to desorb as a supplementary supply. Thus the declining gas flow rate again increases, resulting in the twin peaks observed in the experiment. The gas flow rate from the organic matter again increases due to the increased effective diffusion caused by the decline in the gas pressure.

4. Results and discussion

4.1. Benchmark numerical model

In this section, the models established in Section 3 are applied as a benchmark numerical model to simulate the interaction between inorganic minerals and organic matter during the gas depletion process. Also, two boundary conditions are investigated in this section - *viz*, the constant stress and constant volume conditions. The gas flow and mechanical boundary conditions are identical to those introduced in Section 3. Material property parameters are collected from the literature (Shabro et al., 2012; Shukla et al., 2013; Chen et al., 2015a, 2019; Eliyahu et al., 2015; Huang et al., 2015) and listed in Table 2 together with the general parameters of Table 1. In the simulations, the parameters are retained constant with only the mechanical boundary conditions on the outer edge being different for the two end-member boundary conditions.

4.2. Investigation of gas flow

4.2.1. Gas flow with different effective diffusion coefficients

As shown in Fig. 8(a), the average gas pressure in the inorganic

Table 1
Parameters of the simulation model for model verification.

Variable	Meaning	Value	Parameter	Value
Experiment conditions collected from Guo et al. (2015) and general parameters				
p_0	Initial gas pressure	29[MPa]	p_{out}	Extraction pressure	2[MPa]
T	Temperature	300[K]	ρ_{sh}	Density of shale	2600[kg/m^3]
μ	Gas Dynamic viscosity	1.8e-5 [$Pa{\cdot}s$]	ρ_{ga}	Gas Density at standard pressure	0.716 [kg/m^3]
R	Molecular gas constant	8.3 [J/(mol·K)]			
Parameters collected from Eliyahu et al. (2015)					
E_{in}	Young's Modulus of inorganic mineral	26[GPa]	α_{in}	Biot coefficient of inorganic mineral	0.8
E_{or}	Young's Modulus of organic matter	6[GPa]	α_{or}	Biot coefficient of organic matter	0.9
Parameters assumed in this work					
ϕ_{or0}	Initial porosity of organic mineral	0.9	ϕ_{in0}	Initial porosity of inorganic mineral	0.01
d_{in0}	Pore diameter in inorganic mineral	200[nm]	k_{in0}	Permeability of inorganic mineral	8e-18 [m^2]
r_{or}	Radius of organic matter	3[um]	d_{or0}	Pore diameter in kerogen inclusion	100 [nm]
r_{in}	Radius of inorganic mineral	40[um]	τ	Tortuosity in organic matter	10
D_{s0}	Initial surface diffusion coefficient	1e-12[m^2/s]			

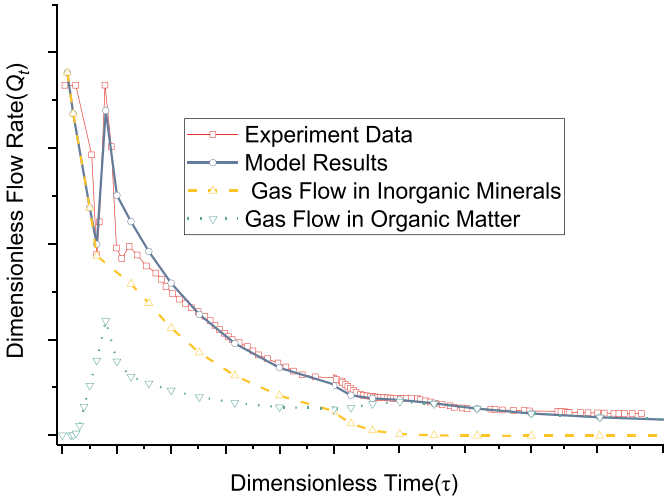

Fig. 7. Comparisons between experimental observations and model.

minerals decreases rapidly to the extraction pressure followed by the average gas pressure in the organic matter until it reaches the extraction pressure. Comparing Fig. 8(b) and Fig. 7, we observe that the appearance of the two peaks in the flow rate depends on the contrast in flow characteristics of the two components. The initial rates are uniform for the different effective diffusion coefficient models while the late production profiles differ as shown in Fig. 8(b). For the varied effective diffusion models, the following features can be observed: (a) the gas pressure of the organic matter calculated by the Walko model declines the most rapidly; (b) the gas pressure and flow rate profile are the same between the Dongari model, Geng model with the big b value ($b = 4$) and Scott model.

Table 2
Parameters for the benchmark numerical model.

	Parameter	Value	Parameter	Value
r_{or}	Radius of kerogen inclusion	3[um]	r_{in}	Radius of inorganic mineral	20[um]
p_0	Initial gas pressure	20 [MPa]	p_{out}	Extraction pressure	1[MPa]
d_{in0}	Pore diameter in inorganic mineral	100 [nm]	k_{in0}	Permeability of inorganic mineral	1e-18 [m^2]
E_{in}	Young's Modulus of inorganic mineral	26 [GPa]	ϕ_{in0}	Initial porosity of inorganic mineral	0.05
α_{in}	Biot coefficient of inorganic mineral	0.8	d_{or0}	Pore diameter in organic matter	10[nm]
E_{or}	Young's Modulus of organic matter	8 [GPa]	ϕ_{or0}	Initial porosity of organic matter	0.6
α_{or}	Biot coefficient of organic matter	0.8	D_{s0}	Initial surface diffusion coefficient	2e-12[m^2/s]
ζ	Interpolation constant in Dongari model	-1	τ	Tortuosity in organic matter	10
T	Temperature	300 [K]	b	Ratio coefficient in Geng Model	1 and 4

4.2.2. Diffusion coefficient and permeability evolution with declining gas pressure

As shown in Fig. 9, the effective diffusion coefficient increases while the surface diffusion coefficient decreases with a decline in gas pressure. The increase of the effective diffusion coefficient is caused by the increased Knudsen number, and the decrease of the surface diffusion coefficient results from the decline in surface coverage. For the inorganic permeability value, it also increases with the decline in gas pressure due to the gas slippage effect. As observed in some experiments (Pan et al., 2015; Cui et al., 2018b), the permeability at lower gas pressures may be ten times higher than that at higher gas pressure. This may be due to the increased gas diffusion in the organic matter.

4.3. Impact of effective strain on permeability evolution of inorganic minerals

The permeability evolution of the inorganic minerals under the contrasting boundary conditions are studied. The results are illustrated in Fig. 10 and the contributions of different mechanisms are also shown. The global strain is the resultant of the volumetric strain (ε_{inv}) of inorganic minerals and the internal strain (ε_{or2in}) between two components. The pressure strain represents the strain caused by the variations of gas pressure serving as local strain. In both conditions, the permeabilities of the inorganic minerals decrease as a result of the compressive strain applied by the organic matter, and the decrease in the pressure strain. For the constant volume condition, the global strain is not zero due to the compressive strain applied by the organic matter. Also, we find that the permeability is higher under the constant volume condition than that under the constant stress condition, extensively as a result of the fixed boundary.

4.4. Impacts of effective strain on effective diffusion under the constant stress condition

Changes in effective strain under the constant stress condition are discussed, and their impacts on the effective diffusion coefficient are investigated.

4.4.1. General pattern of effective diffusion coefficient under the constant stress condition

Fig. 11 represents the evolution of the effective diffusion coefficient under the constant stress condition. As illustrated in the image, the profile of the effective diffusion coefficient is mainly determined by three factors: the global strain applied by both the inorganic minerals and the outer boundary, the decreased gas pressure, and gas desorption

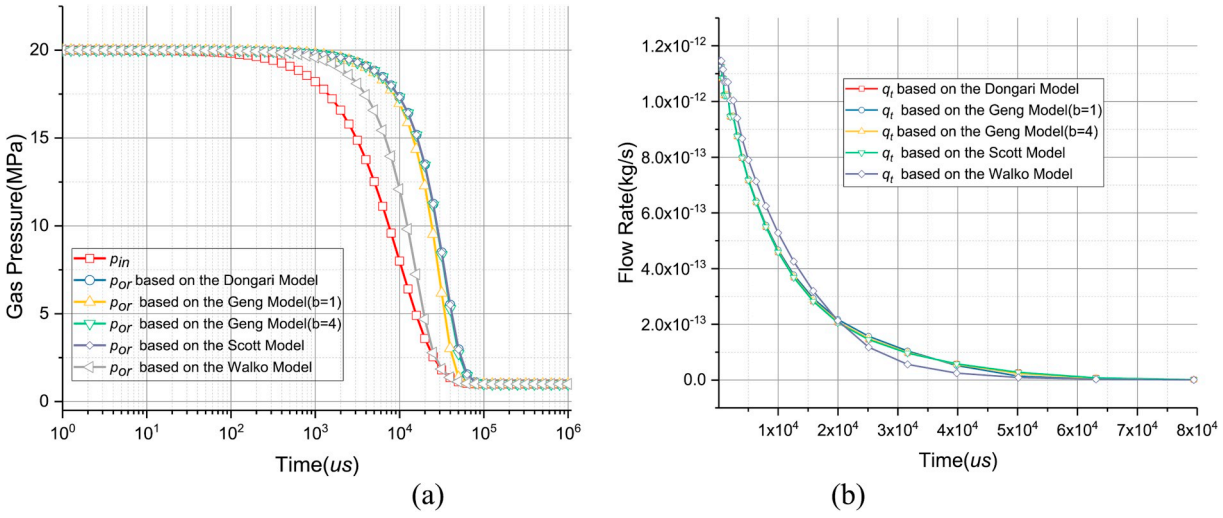

Fig. 8. Illustration of gas flows during the gas depletion process. (a) evolution of gas pressure, p_{in} and p_{or} are the average gas pressure of the inorganic minerals and organic matter, respectively and (b) variation of flow rate (q_t).

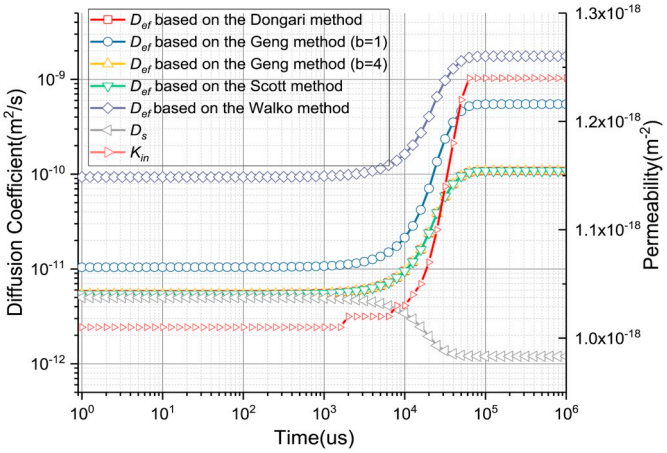

Fig. 9. Evolution of diffusion coefficient and inorganic permeability during the gas depletion process.

in the organic matter. Over the full depletion time scale, the first term acts earliest as it is mainly caused by the decline in gas pressure in the inorganic minerals. The last two terms evolve later as they are mainly activated by gas depletion in the organic matter.

Superposing the three influencing factors, the behavior of the effective diffusion coefficient evolves through three stages: (1) Diffusion Coefficient Decrease. Diffusion coefficient decreases immediately following gas depletion due to the compressive global strain applied by the outer boundary; (2) Diffusion Coefficient Increases. Diffusion coefficient increases after the gas pressure in the inorganic minerals reaches the minimum value. As the gas in the inorganic minerals flows out, the organic matter swells. Also, the gas desorption in the organic matter enlarges the porosity; (3) Diffusion Coefficient Recovery. In the final stage, the gas in the organic matter fully depletes and the pores in the organic matter are compressed according to the effective stress principle. The timing and appearance of the three stages are determined by the values of the various coefficients and their related time of action.

4.4.2. *Impacts of Young's modulus under the constant stress condition*

The impacts of Young's modulus of each inorganic and organic component are investigated as shown in Fig. 12(a) and Fig. 12(b). It should be noted that high Young's modulus also means a high bulk

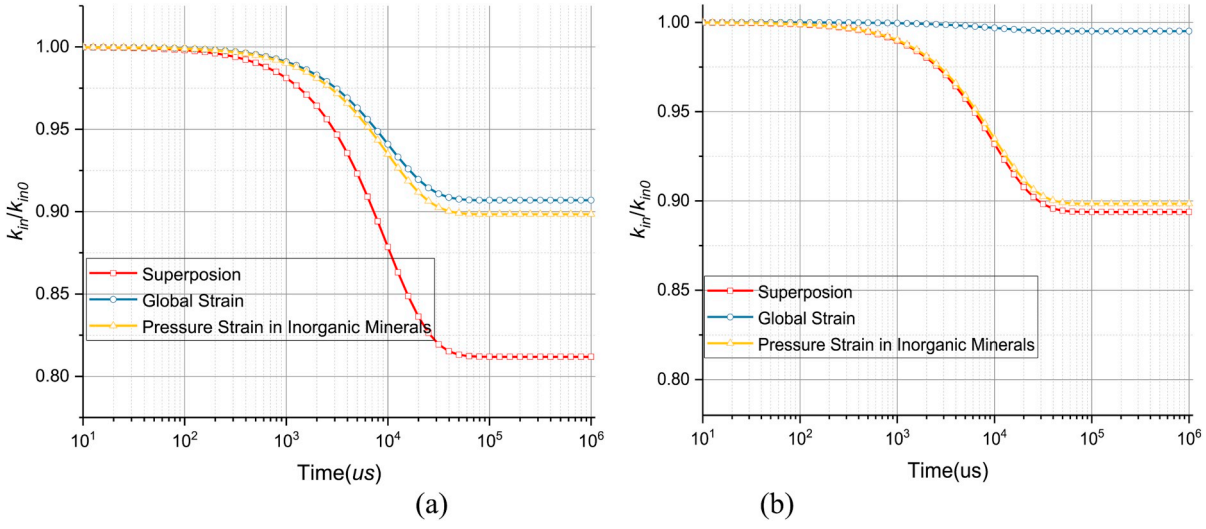

Fig. 10. The permeability evolution of inorganic minerals under (a) constant stress condition and (b) constant volume condition.

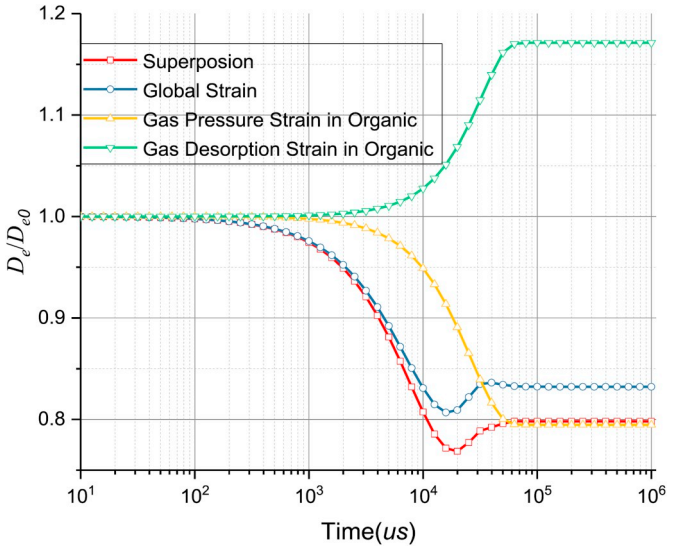

Fig. 11. Evolution of effective diffusion coefficient under the constant stress condition at $E_{in} = 26$ GPa.

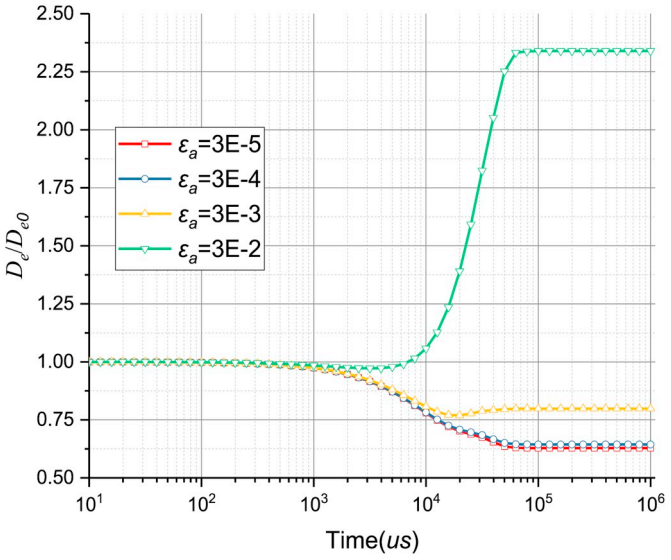

Fig. 13. Influence of adsorptive strain constant under conditions of constant stress.

modulus and the adsorption strain is retained constant in this case. Generally, the lower Young's modulus leads to larger deformation and also a larger change in the effective diffusion coefficient. In other words, the change in the diffusion coefficient is more sensitive to the smaller Young's modulus.

The compressive global strain and the strain resulting from the gas pressure have little impact for the high Young's modulus and the adsorptive strain is dominant. For the cases with low Young's modulus, both strains are dominant while the impact of gas adsorption can be ignored. This indicates that for the REV with high Young's modulus the evolution of effective diffusion coefficient is mainly determined by the internal response, while for the case with low Young's modulus the outer boundary has a significant impact.

4.4.3. Impacts of adsorptive strain under the constant stress condition

As illustrated above, the decreased adsorptive strain increases the effective diffusion coefficient. For simplicity, we define the adsorptive strain constant as $\varepsilon_a = R*T*L$ and the evolution of the diffusion coefficient with varying adsorptive strain constant is illustrated in Fig. 13. As can be observed, the diffusion coefficient subject to high adsorptive strain is significantly enhanced. For the case with low adsorptive strain, the impact of gas adsorption strain can be largely ignored.

4.5. Impact of effective strain on effective diffusion under the constant volume condition

4.5.1. General pattern of effective diffusion coefficient under the constant volume condition

The evolution of the effective diffusion coefficient and the contributions of different mechanisms under the constant volume condition are illustrated in Fig. 14. The difference between the two boundary conditions is that the organic matter will swell at early time (constant volume) instead of being compressed under the constant stress. The impacts of the decreased gas pressure and gas desorption in the organic matter are the same as for the constant stress condition.

Three stages of behavior are observed: (1) Diffusion Coefficient Increase. The gas pressure in the inorganic pores acts as a confining pressure on the organic matter. Thus, the diffusion coefficient increases because of the decreased gas pressure in the inorganic pores; (2) Diffusion Coefficient Decrease. In this stage, the diffusion coefficient

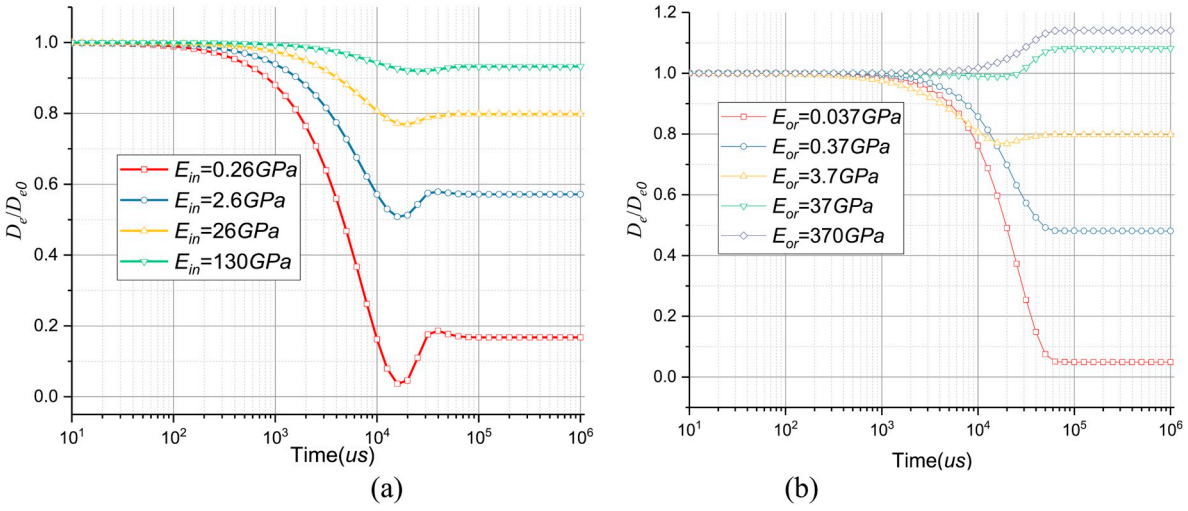

Fig. 12. Influence of Young's Modulus under constant stress for the (a) inorganic minerals and (b) organic matter.

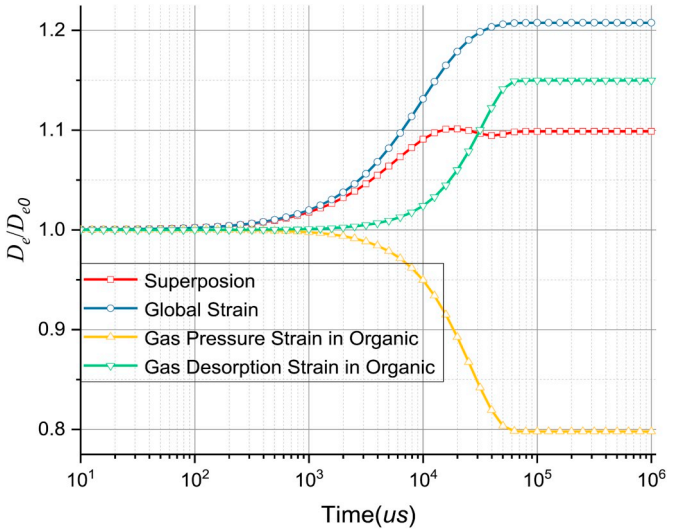

Fig. 14. Evolution of effective diffusion coefficient under the constant volume condition at $E_{in} = 26$ GPa.

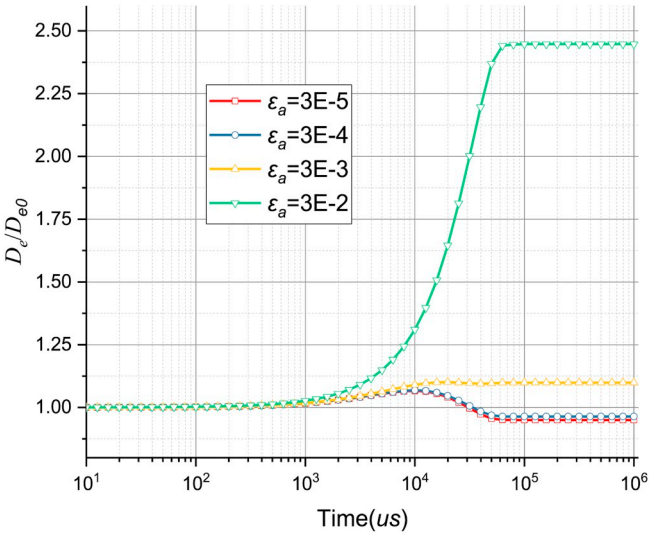

Fig. 16. Impacts of adsorptive strain under the constant volume condition.

decreases due to the decreased gas pressure in the organic matter. As the gas pressure declines, the pores shrink and the organic matter is compressed; (3) Diffusion Coefficient Recovery. In this stage, the gas desorption increases the porosity in the organic matter.

4.5.2. Influence of Young's modulus under the constant volume condition

Fig. 15 represents the variations of the effective diffusion coefficient for different Young's Moduli under the constant volume condition. Similarly, the lower Young's modulus results in a larger deformation and a larger change in the diffusion coefficient. Contrary to the constant stress condition, the lower Young's modulus of the inorganic system increases the diffusion coefficient because it results in a larger swelling volume of the organic matter.

Where the organic matter has a high stiffness ($E_{or} = 37$ GPa or higher), the outer boundary has little impact and only the adsorptive strain exerts an impact. For low stiffness ($E_{or} = 0.37$ GPa or lower) the fixed outer boundary results in decreased gas pressure exerting a significant role.

4.5.3. Influence of adsorptive strain under the constant volume condition

Similar to the constant stress condition, a high gas adsorptive strain increases the diffusion coefficient as illustrated in Fig. 16. For the high adsorptive strain, the final values are almost identical for both constant volume and constant stress conditions. Also, the effect of the adsorptive strain can be neglected where it is small.

4.6. Application of the numerical model

We have proposed a discrete embedded small-scale model as a component REV to evaluate the interactions between inorganic minerals and organic matter. There are three approaches to upscale our small component REV model to large scale.

(1) As noted previously, conventional DP/DK models (Zhao et al., 2014; Peng et al., 2015) are usually applied to simulate the shale gas production behavior and to history match field data. In such approaches, the mass transport and effective stress transfer between sub-systems are simplified to consider only the gas pressure difference with the impacts of effective stress gradients necessarily ignored. The discrete small-scale model gives an explicit method to calculate the interactions between inorganic mineral and organic matter in the shale matrix. The results of this work can be treated as a supplement to the conventional

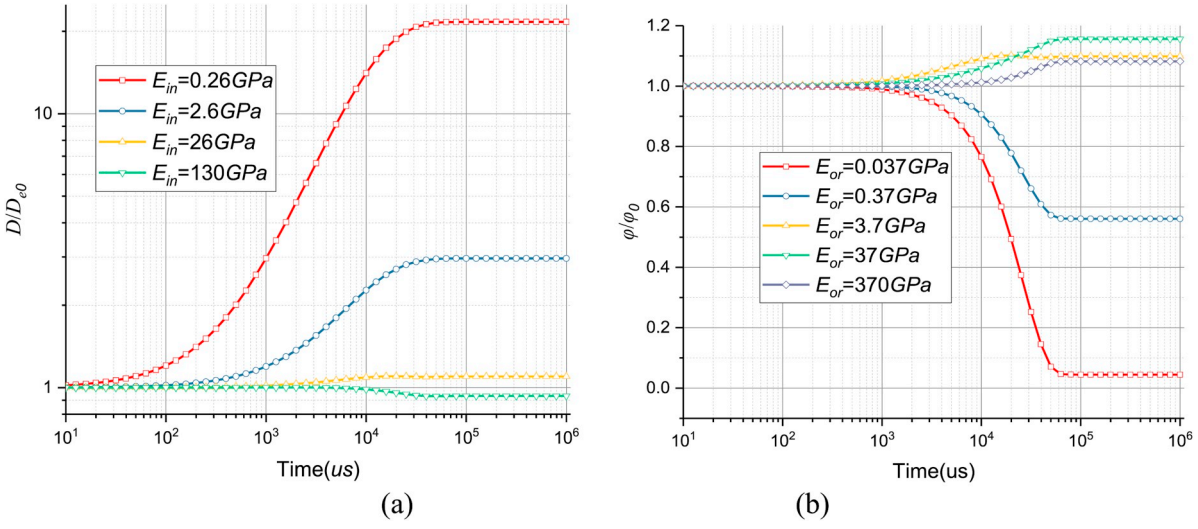

Fig. 15. Influence of Young's Modulus under the condition of constant stress for the (a) inorganic minerals and (b) organic matter.

continuous dual-media approach. In other words, conventional DP/DK models may be upgraded to fully consider the interactions between sub-systems and accurately simulate the shale gas production behavior with the fresh perspective provided by this work.

(2) In the model verification process of this work, a major assumption is that the shale sample comprises only inorganic mineral and organic matter components with no visible fractures – the role of fractures is ignored. Also, the dimensionless time and dimensionless gas rate are used to define the scale effect. A similar approach can also be applied to the field, as the gas stored in the shale matrix serves as the main contributor to long-term gas production behavior. The experimental data first exhibit a decrease and then increase, exhibiting a brief oscillation. This similar trend is also observed in the field data such as the data of Barnett well 3 (Mattar et al., 2008), Marcellus Well #10096 (Esmaili and Mohaghegh, 2016) and Marcellus Well #10032 (Esmaili and Mohaghegh, 2016). In all three gas field data sets, the gas production rate increases following an early sharp decline. Our previous work explicitly identifies this response through a Gaussian Decomposition Method (Cui et al., 2018c) applied as a phenomenological model to history match the data. In this work, we propose a new approach to simulate and explain these filed data on an explicit physical basis.

(3) Besides the ultra-low permeability and porosity, the gas shale reservoir also exhibits high permeability anisotropy -the permeability is directional and the permeability in the horizontal direction is much higher than that in the vertical direction. This anisotropy is one of the key factors in controlling gas flow and gas production rates. As discussed above, the mechanical condition in the horizontal direction can be assumed as the constant volume condition with a constant stress condition in the vertical direction. The permeability in one specific direction is defined as the function of the fracture aperture change in the other directions (Swami and Settari, 2012). For example, when the vertical stress decreases, the aperture in horizontal direction increases and the horizontal permeability is enhanced. In such condition, the evolution of horizontal permeability may follow the law under the condition of constant stress while the evolution of vertical permeability may obey the law under the condition of constant volume.

5. Conclusions

The previous presents a micro-scale discrete coupled model to investigate the coupling between mechanical deformation and flow characteristics in the shale matrix. In the model, the two sub-systems of the shale matrix (inorganic minerals and organic matter) are explicitly defined and the mass transfer and mechanical interaction between them are calculated in an explicit way. Results from a coupled desorption-diffusion-seepage experiment are used to validate the numerical modeling results. Methods of upscaling of the discrete small-scale model are also introduced in the work. The proposed model gives a complementary alternative to the conventional continuous dual-media approach whereby the organic components are physically nested and embedded within an exterior of mineral matter. This model is applied to history match filed data, and in particular to provide a mechanism for the oscillatory gas production data at early time, typically observed in field data. The main conclusions are summarized below:

(1) The impacts of gas pressure on the gas flow characteristics are monotonic. A decline in gas pressure increases the permeability of the inorganic material due to the gas slippage effect. For diffusion in the organic matter, the effective diffusion coefficient increases with a decrease in gas pressure while the surface diffusion coefficient decreases;

(2) The impact of the mechanical deformation on the gas flow characteristics are dynamic and depend on the outer boundary condition and the mechanical interaction between inorganic minerals and organic matter. The intrinsic permeability of the inorganic minerals decreases despite the outer boundary condition. For effective diffusion in the organic matter, the effective diffusion coefficient increases under the constant volume condition and decreases under the constant stress condition, relative to the initial equilibrium magnitude.

(3) The impacts of the elastic modulus and gas adsorptive strain are also investigated. For the case with a high elastic modulus, the impact of the outer boundary can be ignored, and the interior response controls the evolution of transport characteristics of both components. For the case with a low adsorptive strain, the impacts of adsorption strain can be functionally ignored.

Acknowledgments

This work is a partial result of funding by the Natural Science Foundation of China (51609038), the 111 Project (B17009), and the Fundamental Research Funds for the Central Universities (Grant No. N180104021, Grant No. N160104002).

Appendix A. Modified Darcy Flow in Inorganic Minerals

The mass conservation law in the inorganic minerals is:

$$\frac{\partial m_{in}}{\partial t} + \nabla\cdot(\rho_{in}u_{in}) = Q_{sin} \tag{A.1}$$

where m_{in} is the gas mass in the inorganic minerals containing free gas, and Q_{sin} is the mass source term.

The modified Darcy flow is applied to calculate the velocity:

$$u_{in} = -\frac{k_{apin}}{\mu}\nabla p_{in} \tag{A.2}$$

where p_{in} is the gas pressure in the inorganic matrix, k_{apin} is the apparent permeability of inorganic minerals and written as (Zhang et al., 2014):

$$k_{apin} = (1 + \frac{4Kn_{in}}{1 + Kn_{in}})k_{in} \tag{A.3}$$

in which Kn_{in} is the Knudsen number and ρ_{in} is the gas density in inorganic minerals:

$$\rho_{in} = \frac{p_{in}}{p_{ga}}\rho_{ga} \tag{A.4}$$

where p_{ga} is standard atmospheric pressure and ρ_{ga} is the gas density at standard atmospheric pressure. Only free gas exits in the inorganic pores:

$$m_{in} = \rho_{in}\phi_{in} \tag{A.5}$$

where ϕ_{in} is the porosity in inorganic pores. Therefore the gas flow in inorganic minerals can be written as:

$$\frac{\partial}{\partial t}\left(\frac{p_{in}}{p_{ga}}\rho_{ga}\phi_{in}\right) + \nabla\cdot\left(-\frac{p_{in}}{p_{ga}}\rho_{ga}\frac{k_{apin}}{\mu}\nabla p_{in}\right) = Q_{sin} \tag{A.6}$$

Appendix B. Gas Diffusion in Organic Matter

B.1 Bulk Diffusion and Knudsen Diffusion

The mass conservation law in the organic matter is:

$$\frac{\partial m_{or}}{\partial t} + \nabla\cdot J_{or} = Q_{sor} \tag{B.1}$$

where J_{or} is the mass flux in the kerogen system, Q_{sor} is the mass source term, m_{or} is the gas mass in the organic matter and contains both free gas and adsorbed gas. Therefore we can get (Wang et al., 2012):

$$m_{or} = \rho_{or}\phi_{or} + \rho_{ga}\rho_s\frac{L_{or}B_{or}p_{or}}{1 + B_{or}p_{or}} \tag{B.2}$$

As mentioned above, the mass flux (J_{or}) is the superposition of the effective diffusion (the combination of bulk diffusion and Knudsen diffusion) and surface diffusion. As the Knudsen number becomes larger than 10 ($Kn > 10$), mean free path of gas molecules is large or in the same level with pore radius. And the diffusion coefficient of Knudsen diffusion is expressed as (Dongari et al., 2009):

$$D_{or} = \frac{1}{3}u_m d_{or} \tag{B.3}$$

in which d_{or} is the pore diameter in kerogen inclusions. u_m is the arithmetic average of gas velocity is (Geng et al., 2016):

$$u_m = \sqrt{\frac{8RT}{\pi M_g}} \tag{B.4}$$

Considering the effect of porosity, tortuosity, and the roughness, Eq. (B.3) becomes (Darabi et al., 2012; Miao et al., 2018):

$$D^e_{or} = \frac{\phi_{or}}{\tau_{or}}(\delta')^{D_f-2}D_{or} \tag{B.5}$$

where D_f is a dimensionless constant number representing the fractal dimension of the pore wall, δ is also a dimensionless number defined as the ratio of the gas-molecule diameter to the local average pore diameter, ϕ_{or} and τ_{or} are the porosity and tortuosity of the organic matter, respectively.

For the single pure gas with self-diffusion, the bulk diffusion coefficient can be obtained from the molecules kinetic theory and is written as (Dongari et al., 2009):

$$D_b = \frac{1}{3}u_m\lambda = \frac{1}{3}u_m\frac{\lambda}{d_{or}}d_{or} = KnD_{or} \tag{B.6}$$

Considering the effect of porosity and tortuosity, Eq. (B.6) becomes (Darabi et al., 2012; Miao et al., 2018):

$$D^e_b = \frac{\phi_{or}}{\tau_{or}}KnD_{or} \tag{B.7}$$

B.2 Effective Diffusion Coefficient

Geng et al. (2016) proposed a method to calculate the effective diffusion coefficient which makes the bulk diffusion to Knudsen diffusion transition smooth. In his method, the effective diffusion coefficient is calculated as:

$$D^e_{ef} = \frac{\alpha Kn_{or}D^e_{or} + D^e_b}{\alpha Kn_{or} + 1} \tag{B.8}$$

when $Kn \to 0$ it becomes bulk diffusion while when $Kn \to \infty$ it becomes Knudsen diffusion. Also, α is not a constant and depends on the Knudsen number: $\alpha = Kn^b_{or}$ where b is called the ratio coefficient and $b > 0$.

Dongari et al. (2009) proposed a general way to calculate the effective diffusion coefficient:

$$D^e_{ef} = \left((D^e_{or})^\zeta + (D^e_b)^\zeta\right)^{1/\zeta} \tag{B.9}$$

where ζ is interpolation constant. In the case of $\zeta = -1$, effective diffusion becomes Knudsen diffusion and bulk diffusion when $Kn > 10$ and $Kn < 0.01$ (Dongari et al., 2009). Thus $\zeta = -1$ is applied in this work.

Another method combining the bulk diffusion and Knudsen diffusion is the application of probability function which is proposed to calculate the proportion of molecular-molecular or molecular-wall collision in total gas collisions (Wakao et al., 1965; Hashemifard et al., 2013b):

$$\omega = \frac{\text{Wall collision frequency}}{\text{Total collision frequency}} \tag{B.10}$$

In 1962, Scott and Dullien (1962) proposed a method to calculate the probability function of collisions: $\omega = \exp[-\sinh(1/Kn_{or})]$. Another widely used probability function of collisions was introduced by Wakao et al. (1965): $\omega = \frac{Kn_{or}}{1+Kn_{or}}$.

The effective diffusion coefficient becomes:

$$D^e_{ef} = \omega_{or} D^e_{or} + (1 - \omega_{or}) D^e_b \tag{B.11}$$

which is a special case of Geng and Li model ($b = 0$).

B.3 Surface Diffusion

Surface diffusion is caused by the chemical potential gradient of the adsorption phase which related to the gas pressure and temperature. In this work, only the isothermal condition is considered. Based on the Langmuir adsorption theory, the amount of adsorbed gas can be written as:

$$C = C_{max}\theta \text{ and } \theta = \frac{p}{p + P_L} \tag{B.12}$$

where θ is the surface coverage of the adsorption layer and P_L is the Langmuir pressure. Chen and Yang (1991) proposed a kinetic model to calculate the surface diffusion coefficient based on the random walk:

$$\frac{D_s}{D_{s_0}} = \frac{(1-\theta) + \frac{k}{2}\theta(2-\theta) + \{H(1-k)\}(1-k)\frac{k}{2}\theta^2}{(1 - \theta + \frac{k}{2}\theta^2)} \tag{B.13}$$

where k is the dimensionless molecular block coefficient, $H(1\text{-}k)$ is the dimensionless Heaviside function. In surface diffusion, no blockage is expected due to the unlimited space and $k = 0$, we can expect that:

$$\frac{D_s}{D_{s_0}} = \frac{1}{1-\theta} \tag{B.14}$$

Appendix C. Supplementary data

Supplementary data to this article can be found online at https://doi.org/10.1016/j.petrol.2019.106524.

References

Abdassah, D., Ershaghi, I., 1986. Triple-porosity systems for representing naturally fractured reservoirs. SPE Form. Eval. 1 (2), 113–127.

Akkutlu, I.Y., Fathi, E., 2012. Multiscale gas transport in shales with local kerogen heterogeneities. SPE J. 17 (4), 1002–1011.

Ambrose, R.J., Hartman, R.C., Campos, M.D., Akkutlu, I.Y., Sondergeld, C., 2010. New pore-scale considerations for shale gas in place calculations. In: SPE Unconventional Gas Conference, Pittsburgh, Pennsylvania, USA. Society of Petroleum Engineers.

Azom, P.N., Javadpour, F., 2012. Dual-continuum modeling of shale and tight gas reservoirs. In: SPE Annual Technical Conference and Exhibition. San Antonio, Texas, USA. Society of Petroleum Engineers.

Castillo, F., Aguilera, R., Lawton, D., 2011. Integration of seismic data and a triple porosity model for interpretation of tight gas formations in the western Canada sedimentary basin. In: Canadian Unconventional Resources Conference. Calgary, Alberta. Canada, Society of Petroleum Engineers.

Chen, Y.D., Yang, R.T., 1991. Concentration dependence of surface diffusion and zeolitic diffusion. AIChE J. 37 (10), 1579–1582.

Chen, C., Hu, D., Westacott, D., Loveless, D., 2013. Nanometer-scale characterization of microscopic pores in shale kerogen by image analysis and pore-scale modeling. Geochem. Geophys. Geosyst. 14 (10), 4066–4075.

Chen, F., Duan, Y., Wang, K., Li, X., Liao, Y., 2015. A novel pressure transient response model considering multiple migration mechanisms in shale gas reservoir. J. Nat. Gas Sci. Eng. 22, 321–334.

Chen, T., Feng, X.-T., Pan, Z., 2015. Experimental study of swelling of organic rich shale in methane. Int. J. Coal Geol. 150–151, 64–73.

Chen, T., Feng, X.-T., Pan, Z., 2018. Experimental study on kinetic swelling of organic-rich shale in CO_2, CH_4 and N_2. J. Nat. Gas Sci. Eng. 55, 406–417.

Chen, T., Feng, X.-T., Cui, G., Tan, Y., Pan, Z., 2019. Experimental study of permeability change of organic-rich gas shales under high effective stress. J. Nat. Gas Sci. Eng. 64, 1–14.

Coussy, O., 2004. Poromechanics. John Wiley & Sons.

Cui, G., Liu, J., Wei, M., Feng, X., Elsworth, D., 2018. Evolution of permeability during the process of shale gas extraction. J. Nat. Gas Sci. Eng. 49, 94–109.

Cui, G., Liu, J., Wei, M., Shi, R., Elsworth, D., 2018. Why shale permeability changes under variable effective stresses: new insights. Fuel 213, 55–71.

Cui, G., Zhao, Y., Liu, J., Wei, M., Elsworth, D., 2018. A Gaussian decomposition method and its applications to the prediction of shale gas production. Fuel 224, 331–347.

Curtis, M.E., Cardott, B.J., Sondergeld, C.H., Rai, C.S., 2012. Development of organic porosity in the woodford shale with increasing thermal maturity. Int. J. Coal Geol. 103, 26–31.

Darabi, H., Ettehad, A., Javadpour, F., Sepehrnoori, K., 2012. Gas flow in ultra-tight shale strata. J. Fluid Mech. 710, 641–658.

Dongari, N., Sharma, A., Durst, F., 2009. Pressure-driven diffusive gas flows in micro-channels: from the Knudsen to the continuum regimes. Microfluid. Nanofluidics 6 (5), 679–692.

EIA., 2016. U.S. Energy Information Administration Annual Energy Outlook 2016.

Eliyahu, M., Emmanuel, S., Day-Stirrat, R.J., Macaulay, C.I., 2015. Mechanical properties of organic matter in shales mapped at the nanometer scale. Mar. Pet. Geol. 59, 294–304.

Emmanuel, S., Eliyahu, M., Day-Stirrat, R.J., Hofmann, R., Macaulay, C.I., 2016. Impact of thermal maturation on nano-scale elastic properties of organic matter in shales. Mar. Pet. Geol. 70, 175–184.

Esmaili, S., Mohaghegh, S.D., 2016. Full field reservoir modeling of shale assets using advanced data-driven analytics. Geosci. Front. 7 (1), 11–20.

Fathi, E., Akkutlu, I.Y., 2009. Matrix heterogeneity effects on gas transport and adsorption in coalbed and shale gas reservoirs. Transp. Porous Media 80 (2), 281–304.

Gale, J.F.W., Reed, R.M., Holder, J., 2007. Natural fractures in the Barnett shale and their importance for hydraulic fracture treatments. AAPG Bull. 91 (4), 603–622.

Geng, L., Li, G., Zitha, P., Tian, S., Sheng, M., Fan, X., 2016. A diffusion–viscous flow model for simulating shale gas transport in nano-pores. Fuel 181, 887–894.

Guo, W., Zhiming, H., Luo, Z., Shufeng, G., Rongze, Y., Bo, Z., 2015. Gas desorption-diffusion-seepage coupled experiment of shale matrix and mathematic model. Chin. J. Theor. Appl. Mech. 47 (6), 916–922.

Haghshenas, B., Clarkson, C.R., Chen, S., 2013. Multi-porosity, multi-permeability models for shale gas reservoirs. In: SPE Unconventional Resources Conference Canada. Society of Petroleum Engineers, Alberta, Canada.

Hashemifard, S.A., Ismail, A.F., Matsuura, T., 2013. To what extent the conventional gas permeation testing method is reliable for membrane systems? Separ. Purif. Technol. 114 (32), 90–98.
Heidug, W.K., Wong, S.W., 1996. Hydration swelling of water-absorbing rocks: a constitutive model. Int. J. Numer. Anal. Methods 20 (6), 403–430.
Huang, T., Guo, X., Chen, F.F., 2015. Modeling transient flow behavior of a multiscale triple porosity model for shale gas reservoirs. J. Nat. Gas Sci. Eng. 23, 33–46.
Javadpour, F., 2009. Nanopores and apparent permeability of gas flow in mudrocks (shales and siltstone). J. Can. Pet. Technol. 48 (8), 16–21.
Kumar, H., Elsworth, D., Mathews, J.P., Marone, C., 2016. Permeability evolution in sorbing media: analogies between organic-rich shale and coal. Geofluids 16 (1), 43–55.
Li, S., Dong, M., Li, Z., 2009. Measurement and revised interpretation of gas flow behavior in tight reservoir cores. J. Pet. Sci. Eng. 65 (1–2), 81–88.
Liu, J., Chen, Z., Elsworth, D., Miao, X., Mao, X., 2011. Evolution of coal permeability from stress-controlled to displacement-controlled swelling conditions. Fuel 90 (10), 2987–2997.
Loucks, R.G., Reed, R.M., Ruppel, S.C., Jarvie, D.M., 2009. Morphology, genesis, and distribution of nanometer-scale pores in siliceous mudstones of the mississippian Barnett shale. J. Sediment. Res. 79 (12), 848–861.
Liu, J., Chen, Z., Elsworth, D., Qu, H., Chen, D., 2011. Interactions of multiple processes during cbm extraction: a critical review. Int. J. Coal Geol. 87 (3–4), 175–189.
Loucks, R.G., Reed, R.M., Ruppel, S.C., Hammes, U., 2012. Spectrum of pore types and networks in mudrocks and a descriptive classification for matrix-related mudrock pores. AAPG Bull. 96 (6), 1071–1098.
Ma, Q., Harpalani, S., Liu, S., 2011. A simplified permeability model for coalbed methane reservoirs based on matchstick strain and constant volume theory. Int. J. Coal Geol. 85 (1), 43–48.
Mattar, L., 2008. Production analysis and forecasting of shale gas reservoirs: case history-based approach. In: SPE Shale Gas Production Conference. Fort Worth, Texas, USA. Society of Petroleum Engineers.
Mehmani, A., Prodanović, M., Javadpour, F., 2013. Multiscale, Multiphysics network modeling of shale matrix gas flows. Transp. Porous Media 99 (2), 377–390.
Miao, Y., Li, X., Zhou, Y., Lee, J., Sun, Z., Chang, Y., Wang, S., Hou, C., 2018. A new rate-transient analysis model for shale gas reservoirs coupled the effect of slip flow and surface diffusion. Int. J. Heat Mass Transf. 124, 1–10.
Pan, Z., Connell, L.D., 2007. A theoretical model for gas adsorption-induced coal swelling. Int. J. Coal Geol. 69 (4), 243–252.
Pan, Z., Connell, L.D., 2012. Modelling permeability for coal reservoirs: a review of analytical models and testing data. Int. J. Coal Geol. 92, 1–44.
Pan, Z., Connell, L.D., 2015. Reservoir simulation of free and adsorbed gas production from shale. J. Nat. Gas Sci. Eng. 22, 359–370.
Pan, Z., Ma, Y., Danesh, N.N., Connell, L.D., Sander, R., Down, D.I., Camilleri, M., 2015. Measurement of shale anisotropic permeability and its impact on shale gas production. In: SPE Asia Pacific Unconventional Resources Conference and Exhibition. Society of Petroleum Engineers, Brisbane, Australia.
Peng, Y., Liu, J., Wei, M., Pan, Z., Connell, L., 2014. Why coal permeability changes under free swellings: new insights. Int. J. Coal Geol. 133, 35–46.
Peng, Y., Liu, J.S., Pan, Z.J., Connell, L.D., 2015. A sequential model of shale gas transport under the influence of fully coupled multiple processes. J. Nat. Gas Sci. Eng. 27, 808–821.
Peng, Y., Liu, J., Pan, Z., Connell, L.D., Chen, Z., Qu, H., 2017. Impact of coal matrix strains on the evolution of permeability. Fuel 189, 270–283.
Rogers, S., Elmo, D., Dunphy, R., Bearinger, D., 2010. Understanding hydraulic fracture geometry and interactions in the horn river basin through dfn and numerical modeling. Int. J. Sports Med. 31 (7), 458–462.
Roy, S., Raju, R., Chuang, H.F., Cruden, B.A., Meyyappan, M., 2003. Modeling gas flow through microchannels and nanopores. J. Appl. Phys. 93 (8), 4870–4879.
Scott, D.S., Dullien, F.A.L., 1962. The flow of rarefied gases. AIChE J. 8 (3), 293–297.
Shabro, V., Torres-Verdin, C., Sepehrnoori, K., 2012. Forecasting gas production in organic shale with the combined numerical simulation of gas diffusion in kerogen, Langmuir desorption from kerogen surfaces, and advection in nanopores. In: SPE Annual Technical Conference and Exhibition. San Antonio, Texas, USA. Society of Petroleum Engineers.
Shi, J.Q., Durucan, S., 2004. Drawdown induced changes in permeability of coalbeds: a new interpretation of the reservoir response to primary recovery. Transp. Porous Media 56 (1), 1–16.
Shi, R., Liu, J., Wei, M., Elsworth, D., Wang, X., 2018. Mechanistic analysis of coal permeability evolution data under stress-controlled conditions. Int. J. Rock Mech. Min. Sci. 110, 36–47.
Shukla, P., Kumar, V., Curtis, M., Sondergeld, C.H., Rai, C.S., 2013. Nanoindentation studies on shales. In: 47th U.S. Rock Mechanics/Geomechanics Symposium. American Rock Mechanics Association, San Francisco, California.
Song, H., Yu, M., Zhu, W., Wu, P., Lou, Y., Wang, Y., Killough, J., 2015. Numerical investigation of gas flow rate in shale gas reservoirs with nanoporous media. Int. J. Heat Mass Transf. 80, 626–635.
Swami, V., Settari, A., 2012. A pore scale gas flow model for shale gas reservoir. In: SPE Americas Unconventional Resources Conference. Society of Petroleum Engineers, Pittsburgh, Pennsylvania USA.
Tan, Y., Pan, Z., Liu, J., Wu, Y., Haque, A., Connell, L.D., 2017. Experimental study of permeability and its anisotropy for shale fracture supported with proppant. J. Nat. Gas Sci. Eng. 44, 250–264.
Tan, Y., Pan, Z., Liu, J., Feng, X.-T., Connell, L.D., 2018. Laboratory study of proppant on shale fracture permeability and compressibility. Fuel 222, 83–97.
Tan, Y., Pan, Z., Feng, X.-T., Connel, L.D., Li, S., 2019. Laboratory characterisation of fracture compressibility for coal and shale gas reservoir rocks: a review. Int. J. Coal Geol. 204, 1–17.
Tian, H., Pan, L., Xiao, X., Wilkins, R.W.T., Meng, Z., Huang, B., 2013. A preliminary study on the pore characterization of lower silurian black shales in the chuandong thrust fold belt, southwestern China using low pressure N2 adsorption and Fe-sem methods. Mar. Pet. Geol. 48, 8–19.
Vandamme, M., Brochard, L., Coussy, O., Vafai, K., 2010. Adsorption-induced deformation in porous media and application to CO_2-injected coal beds. AIP Conf. Proc. AIP 1254 (1), 319–324.
Wakao, N., Otani, S., Smith, J.M., 1965. Significance of pressure gradients in porous materials: Part I. Diffusion and flow in fine capillaries. AIChE J. 11 (3), 435–439.
Wang, L., Chen, Z., Wang, C., Elsworth, D., Liu, W., 2019. Reassessment of coal permeability evolution using steady-state flow methods: The role of flow regime transition. Int. J. Coal Geol. 211, 1–13.
Wang, J.G., Kabir, A., Liu, J., Chen, Z., 2012. Effects of non-Darcy flow on the performance of coal seam gas wells. Int. J. Coal Geol. 93, 62–74.
Wang, C., Zhai, P., Chen, Z., Liu, J., Wang, L., Xie, J., 2017. Experimental study of coal matrix-cleat interaction under constant volume boundary condition. Int. J. Coal Geol. 181, 124–132.
Warren, J.E., Root, P.J., 1963. The behavior of naturally fractured reservoirs. Soc. Pet. Eng. J. 3 (03), 245–255.
Wasaki, A., Akkutlu, I.Y., 2014. Permeability of organic-rich shale. In: SPE Annual Technical Conference and Exhibition. Amsterdam, The Netherlands. Society of Petroleum Engineers.
Yang, F., Ning, Z., Liu, H., 2014. Fractal characteristics of shales from a shale gas reservoir in the Sichuan basin, China. Fuel 115, 378–384.
Yang, B., Kang, Y., You, L., Li, X., Chen, Q., 2016. Measurement of the surface diffusion coefficient for adsorbed gas in the fine mesopores and micropores of shale organic matter. Fuel 181, 793–804.
Zhang, H., Liu, J., Elsworth, D., 2008. How sorption-induced matrix deformation affects gas flow in coal seams: a new FE model. Int. J. Rock Mech. Min. Sci. 45 (8), 1226–1236.
Zhang, L., Li, D., Li, L., Lu, D., 2014. Development of a new compositional model with multi-component sorption isotherm and slip flow in tight gas reservoirs. J. Nat. Gas Sci. Eng. 21, 1061–1072.
Zhang, S., Liu, J., Wei, M., Elsworth, D., 2018. Coal permeability maps under the influence of multiple coupled processes. Int. J. Coal Geol. 187, 71–82.
Zhao, Y., Zhang, L., Luo, J., Zhang, B., 2014. Performance of fractured horizontal well with stimulated reservoir volume in unconventional gas reservoir. J. Hydrol. 512, 447–456.